GPI spectra of HR8799 c, d, and e in H-K bands with KLIP Forward Modeling

Alexandra Z. Greenbaum,[1] Laurent Pueyo,[2] Jean-Baptiste Ruffio,[3] Jason J. Wang,[4] Robert J. De Rosa,[4] Jonathan Aguilar,[5] Julien Rameau,[6] Travis Barman,[7] Christian Marois,[8,9] Mark S. Marley,[10] Quinn Konopacky,[11] Abhijith Rajan,[12] Bruce Macintosh,[3] Vanessa P. Bailey,[13] Brian Bauman,[14] Joanna Bulger,[15] Adam S. Burrows,[16] Andrew Cardwell,[17] Jeffrey Chilcote,[3,18] Tara Cotten,[19] Daren Dillon,[20] Rene Doyon,[6] Gaspard Duchêne,[4,21] Jennifer Dunn,[8] Darren Erikson,[8] Michael P. Fitzgerald,[22] Katherine B. Follette,[3] Donald Gavel,[20] Stephen J. Goodsell,[23] James R. Graham,[4] Markus Hartung,[17] Pascale Hibon,[17] Li-Wei Hung,[22] Patrick Ingraham,[24] Paul Kalas,[4,25] James E. Larkin,[22] Jérôme Maire,[11] Franck Marchis,[25] James McBride,[4] Stanimir Metchev,[26,27] Maxwell A. Millar-Blanchaer,[13,28] Katie M. Morzinski,[29] Eric L. Nielsen,[25,3] Andrew Norton,[20] Rebecca Oppenheimer,[30] David Palmer,[14] Jennifer Patience,[12] Marshall Perrin,[2] Lisa Poyneer,[14] Fredrik T. Rantakyrö,[17] Naru Sadakuni,[31] Leslie Saddlemyer,[8] Dmitry Savransky,[32] Adam C. Schneider,[12] Andrew Serio,[17] Anand Sivaramakrishnan,[2] Inseok Song,[19] Remi Soummer,[2] Sandrine Thomas,[24] J. Kent Wallace,[13] Kimberly Ward-Duong,[12] Sloane Wiktorowicz,[33] and Schuyler Wolff[5]

[1]Department of Astronomy, University of Michigan, Ann Arbor, MI 48109, USA
[2]Space Telescope Science Institute, Baltimore, MD 21218, USA
[3]Kavli Institute for Particle Astrophysics and Cosmology, Stanford University, Stanford, CA 94305, USA
[4]Department of Astronomy, University of California, Berkeley, CA 94720, USA
[5]Department of Physics and Astronomy, Johns Hopkins University, Baltimore, MD 21218, USA
[6]Institut de Recherche sur les Exoplanètes, Département de Physique, Université de Montréal, Montréal QC, H3C 3J7, Canada
[7]Lunar and Planetary Laboratory, University of Arizona, Tucson AZ 85721, USA
[8]National Research Council of Canada Herzberg, 5071 West Saanich Rd, Victoria, BC, V9E 2E7, Canada
[9]University of Victoria, 3800 Finnerty Rd, Victoria, BC, V8P 5C2, Canada
[10]NASA Ames Research Center, Mountain View, CA 94035, USA
[11]Center for Astrophysics and Space Science, University of California San Diego, La Jolla, CA 92093, USA
[12]School of Earth and Space Exploration, Arizona State University, PO Box 871404, Tempe, AZ 85287, USA
[13]Jet Propulsion Laboratory, California Institute of Technology, Pasadena, CA 91109, USA
[14]Lawrence Livermore National Laboratory, Livermore, CA 94551, USA
[15]Subaru Telescope, NAOJ, 650 North A'ohoku Place, Hilo, HI 96720, USA
[16]Department of Astrophysical Sciences, Princeton University, Princeton NJ 08544, USA
[17]Gemini Observatory, Casilla 603, La Serena, Chile
[18]Department of Physics, University of Notre Dame, 225 Nieuwland Science Hall, Notre Dame, IN, 46556, USA
[19]Department of Physics and Astronomy, University of Georgia, Athens, GA 30602, USA
[20]University of California Observatories/Lick Observatory, University of California, Santa Cruz, CA 95064, USA
[21]Univ. Grenoble Alpes/CNRS, IPAG, F-38000 Grenoble, France
[22]Department of Physics & Astronomy, University of California, Los Angeles, CA 90095, USA
[23]Gemini Observatory, 670 N. A'ohoku Place, Hilo, HI 96720, USA
[24]Large Synoptic Survey Telescope, 950N Cherry Ave., Tucson, AZ 85719, USA
[25]SETI Institute, Carl Sagan Center, 189 Bernardo Ave., Mountain View CA 94043, USA
[26]Department of Physics and Astronomy, Centre for Planetary Science and Exploration, The University of Western Ontario, London, ON N6A 3K7, Canada
[27]Department of Physics and Astronomy, Stony Brook University, Stony Brook, NY 11794-3800, USA
[28]NASA Hubble Fellow
[29]Steward Observatory, University of Arizona, Tucson, AZ 85721, USA
[30]Department of Astrophysics, American Museum of Natural History, New York, NY 10024, USA
[31]Stratospheric Observatory for Infrared Astronomy, Universities Space Research Association, NASA/Armstrong Flight Research Center, 2825 East Avenue P, Palmdale, CA 93550, USA
[32]Sibley School of Mechanical and Aerospace Engineering, Cornell University, Ithaca, NY 14853, USA
[33]Department of Astronomy, UC Santa Cruz, 1156 High St., Santa Cruz, CA 95064, USA

Corresponding author: Alexandra Greenbaum
azgreenb@umich.edu

ABSTRACT

We demonstrate KLIP forward modeling spectral extraction on Gemini Planet Imager coronagraphic data of HR8799, using `PyKLIP`. We report new and re-reduced spectrophotometry of HR8799 c, d, and e from H-K bands. We discuss a strategy for choosing optimal KLIP PSF subtraction parameters by injecting fake sources and recovering them over a range of parameters. The K1/K2 spectra for planets c and d are similar to previously published results from the same dataset. We also present a K band spectrum of HR8799e for the first time and show that our H-band spectra agree well with previously published spectra from the VLT/SPHERE instrument. We compare planets c, d, and e with M, L, and T-type field objects. All objects are consistent with low gravity mid-to-late L dwarfs, however, a lack of standard spectra for low gravity late L-type objects lead to poor fit for gravity. We place our results in context of atmospheric models presented in previous publications and discuss differences in the spectra of the three planets.

Keywords: planets and satellites: gaseous planets – stars: individual (HR8799)

1. INTRODUCTION

Directly imaged planets present excellent laboratories to study the properties of the outer-architectures of young solar systems. Near-infrared spectroscopic follow-up can constrain atmospheric properties including molecular absorption, presence of clouds, and non-equilibrium chemistry (Barman et al. 2011; Konopacky et al. 2013; Marley et al. 2012). Composition, especially in relation to the host star is an important probe of physical processes and formation history (Öberg et al. 2011).

HR8799 has been a testbed for detection techniques (Lafrenière et al. 2009; Soummer et al. 2011, e.g.,), astrometric monitoring and dynamical studies (Fabrycky & Murray-Clay 2010; Soummer et al. 2011; Pueyo et al. 2015; Konopacky et al. 2016; Zurlo et al. 2016; Wertz et al. 2017), atmospheric characterization (Janson et al. 2010; Bowler et al. 2010; Hinz et al. 2010; Barman et al. 2011; Madhusudhan et al. 2011; Currie et al. 2011; Skemer et al. 2012; Marley et al. 2012; Konopacky et al. 2013; Ingraham et al. 2014; Barman et al. 2015; Rajan et al. 2015; Bonnefoy et al. 2016), and even variability (Apai et al. 2016). HR8799 is the only system containing multiple imaged planets, b,c,d, and e, presenting a unique opportunity for studying planet formation. Astrometric monitoring and multiwavelength characterization enable the study of dynamics and composition as a function of mass and semi-major axis.

Spectro-photometry and moderate resolution spectroscopy have provided the first detailed view into the atmospheres of the HR8799 companions. Water and carbon monoxide absorption lines have been detected in the atmospheres of planets b and c, with methane absorption additionally detected in b (Barman et al. 2011; Konopacky et al. 2013; Barman et al. 2015). To account for the discrepancy between the spectra of b and c and those of field objects, previous near-IR observations from 1-5μm have proposed the presence of clouds (Madhusudhan et al. 2011), disequilibrium chemistry to explain an absence of methane absorption (Barman et al. 2011; Konopacky et al. 2013), and even non-solar composition (Lee et al. 2013). However, some work suggests that prescriptions of disequilibrium chemistry, non-solar composition, and/or patchy atmospheres may not play as important role for the d, e planets (Bonnefoy et al. 2016), which appear consistent with dusty late-L objects based on their YJH spectra and SEDs, and can be modeled with atmospheres that do not contain these features.

K band spectra are especially sensitive to atmospheric properties and composition, especially methane and water. The HR8799 planets b, d, and c have shown a lack of methane absorption in the K-band spectra (Bowler et al. 2010; Barman et al. 2011; Currie et al. 2011; Konopacky et al. 2013; Ingraham et al. 2014), inconsistent with field brown dwarf counterparts.

PSF-subtraction algorithms that take advantage of angular and/or spectral diversity, while powerful for removing the stellar PSF, result in self-subtraction of the signal of interest, which can bias the measured astrometry and photometry. Many signal extraction approaches address the effects of self subtraction by injecting a negative fake signal into the data to minimize the detected signal (Marois et al. 2010a; Lagrange et al. 2010, e.g.). In the case of spectral dimension template PSFs of representative spectral types can be used to optimize the extraction/detection (Marois et al. 2010a; Ruffio et al. 2017).

In this paper we present H-K spectra of planets c, d, and e obtained with the Gemini Planet Imager (GPI). We use Karhunen Loéve Image Projection (KLIP) for PSF subtraction with the forward model formalism demonstrated in

Pueyo (2016). In §2.2 we discuss the implementation of KLIP forward modeling (hereafter KLIP-FM) and optimization of KLIP parameters. In §3 we display our spectra next to previous results from Ingraham et al. (2014) and Zurlo et al. (2016); Bonnefoy et al. (2016), and discuss consistencies and discrepancies. We also compare the three object for similarity in their spectra. We compare a library of classified field and low gravity objects to our H and K spectra in §3.2 and report best fit spectral type. Finally, we discuss a few different atmospheric models and their best fits to our spectra in §3.3.

2. OBSERVATIONS AND DATA REDUCTION

2.1. *GPI Observations*

HR8799 was observed with the Gemini Planet Imager Integral Field Spectrograph (IFS) with its K1 and K2 filters on 2013 November 17 (median seeing 0.97 arcsec) and November 18 (median seeing 0.75 arcsec), respectively, during GPI's first light. Conditions are described in detail in Ingraham et al. (2014). During the last 10 exposures of the K1 observations cryocooler power was decreased to 30% to reduce vibration, and the last 14 exposures of the K2 observations had the cryocooler power decreased. Since commissioning the cryocooling system has been upgraded with active dampers to mitigate cryocooler cycle vibrations [Is there an SPIE/other paper that talks about this?]. HR8799 was observed again on September 19 2016 in GPI's H-band (median seeing 0.97 arcsec) as a part of the GPI Expolanet Survey (GPIES) with the updated active damping system. Planet b falls outside the field of view in these data.

Datacube assembly was performed using the GPI Data Reduction Pipeline (DRP) (GPI instrument Collaboration 2014; Perrin et al. 2014). Wavelength calibration for the K1 and K2 data was done using a Xenon arc lamp and flexure offset adjusted manually (Wolff et al. 2014). Bad pixels were corrected and a dark and sky frame were subtracted from the raw data. The raw detector frames were assembled into spectral datacubes. Images were corrected for distortion (Konopacky et al. 2014) and high pass filtered. H-band datacube reduction followed a similar procedure, except that flexure offsets were determined through the bandshift method (**Not sure if this part requires more explanation**).

The instrument transmission function was calibrated using the GPI grid apodizer spots, which place a copy of the stellar PSF in four locations in the image (Sivaramakrishnan & Oppenheimer 2006). These fiducial spots are used to convert raw data counts to contrast units and determine the precise stellar position for relative astrometry (Wang et al. 2014).

2.2. *KLIP forward modeling for unbiased spectra*

PSF subtraction is performed by constructing an optimized combination of reference images with Karhunen-Loéve Image Projection, henceforth KLIP (Soummer et al. 2012). The K-L basis is formed from the covariance matrix of the reference images. To account for over- and self- subtraction of the companion signal we use the approach detailed in Pueyo (2016) to forward model the signal in PSF-subtracted data to recover an unbiased spectrum. The forward model is constructed by perturbing the covariance matrix of the reference library to account for a faint companion signal and propagating this through the KLIP algorithm.

Over- and self-subtraction effects are accounted for in the forward model by projecting a model of the PSF onto the unperturbed KL basis (over-subtraction) and the KL basis perturbation (self-subtraction). For the analysis presented in this paper, the PSF model is constructed from the satellite spots.

After computing the forward model, the spectrum is recovered by solving the inverse problem for f_λ:

Table 1. Summary of observations

DATE	Band	#[a]	Int (s)	Rot[b]	Airmass	Seeing
20131117	K1	24	90	17.1^o	1.62	0.98"
20131118	K2	20	90	9.7^o	1.62	0.72"
20160919	H	60	60	20.9^o	1.61	0.97"

[a]Number of frames
[b]Total sky rotation in the dataset
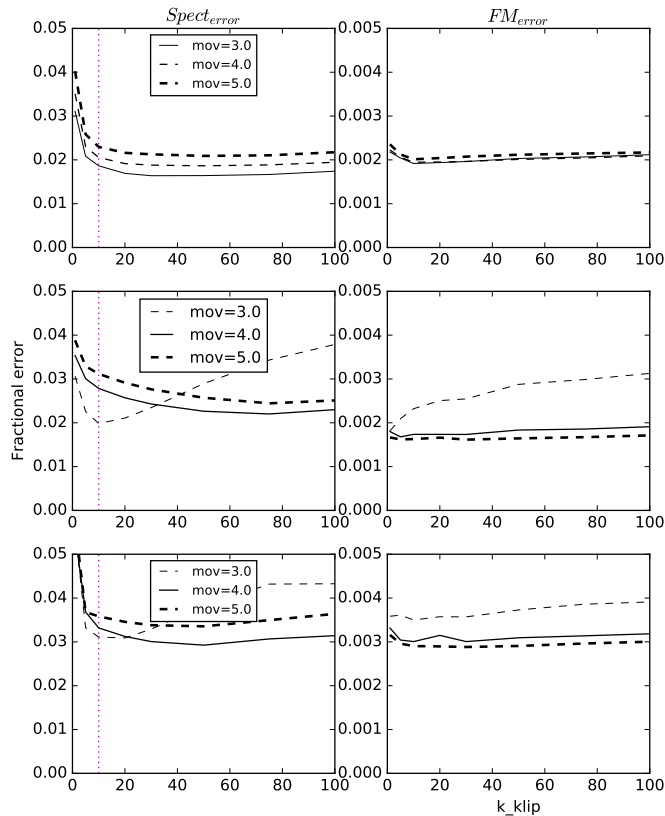
Planet c: H, K1, and K2 by row

Figure 1. Varying KLIP-FM over a range of parameters for planet c. Left: Difference between the measured spectrum at the planet location and the recovered spectra of fake injections, normalized by the recovered spectrum. Right: The variance normalized by the recovered spectrum. The solid line denotes the chosen *mov* value (in pixels). k_{klip} is chosen to minimize the bias at the selected value of *mov*.

$$f_\lambda \cdot \text{FM} = \text{klippeddata} \tag{1}$$

We have tested both pseudoinverse and least squares approaches to inverting the the FM matrix, yielding similar results. We use the pseudoinverse for the results presented in the paper. Both approaches and documentation are available with the `PyKLIP`[1] package.

Using the approximate contrast summed over the bandpass for each object we run Bayesian KLIP Astrometry Wang et al. (2016) to measure the astrometry of each planet in the different datasets. The improved position reduces residuals between the forward model containing the optimized spectrum and the PSF-subtracted data.

We run KLIP-FM spectral extraction with the updated astrometry on a range of KLIP parameters, the KLIP cuttoff k_{klip} and movement, *mov*. *mov* specifies the number of pixels the planet should move between reference library images. Fake signals with the spectrum recovered at the planet location are inserted into the data at the same separation (avoiding the region of the planet). To choose the best algorithm parameters, we consider the error between the fake injection recovery and the input spectrum, as well as the error in the residual pixels in the region of interest. The first term is defined as

$$\text{spect}_{\text{error}} = \frac{1}{N_\lambda N_{fakes}} \sum^{N_\lambda} \sqrt{\frac{\sum_i^{N_{fakes}}(f_\lambda - f'_{\lambda,i})^2}{f_\lambda^2}} \tag{2}$$

[1] http://pyklip.readthedocs.io/

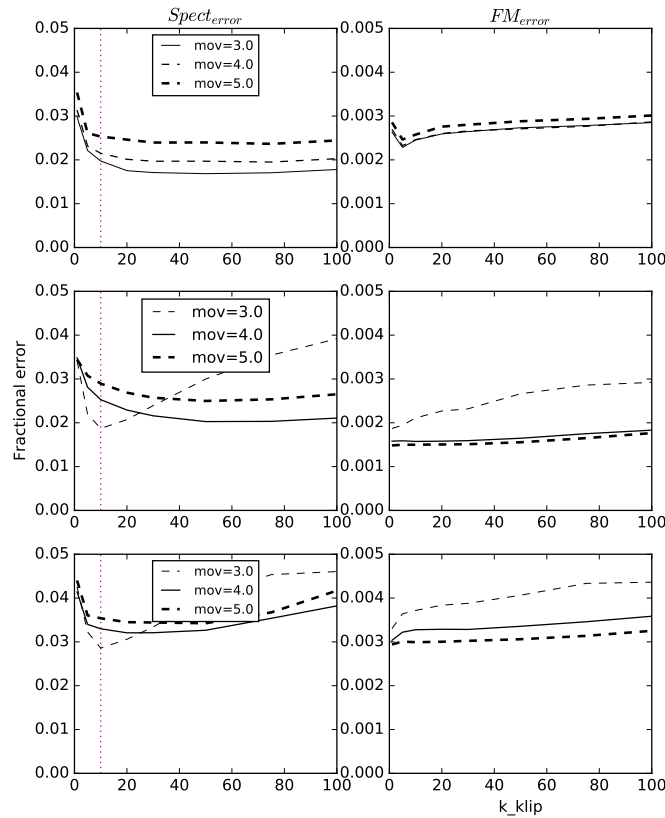## Planet d: H, K1, and K2 by row

Figure 2. Same as Figure 1, but for planet d. The solid line denotes the chosen *mov* value. k_{klip} is chosen to minimize the bias at the selected value of *mov* (pixels).

where f_λ is the spectrum recovered at the location of the planet and $f'_{\lambda,i}$ is the spectrum recovered for the ith fake source. Our images contain 37 wavelength slices per band. We define the residual error as the sum of the residual image pixels squared divided by the sum of the klipped image. The residual is calculated inside a region with a radius of 4 pixels.

$$\text{residual}_\lambda = \text{klipped}_\lambda - \text{forwardmodel}_\lambda,$$

$$\text{FM}_{\text{error}} = \frac{1}{N_\lambda N_{fakes}} \sum^{N_\lambda} \sqrt{\frac{\sum_{pixels} \text{residual}_\lambda{}^2}{\sum_{pixels} \text{klipped}_\lambda{}^2}} \tag{3}$$

Figures 1, 2, and 3 display the spectrum error (left) and residual error (right) for the range of investigated KLIP parameters. The three panels top to bottom show the result for H, K1, and K2 bands. The solid line plotted in each panel represents the value of *mov* chosen for the final spectrum, with the other values of *mov* represented in dashed lines of varying thickness. The dotted vertical magenta line represents the chosen value of k_{klip}.

We choose KLIP parameters that minimize the *spect_error* and prefer solutions with smaller value of k_{klip} that occur before the minimum. As demonstrated in Pueyo (2016) the forward model starts to fail for aggressive (large k_{klip}) reductions of bright signals. The error in the residual is much smaller than our spectrum error, indicating that we are not underestimating our errors by using the recovery of injected signals. Additional work is necessary to develop a more rigorous framework for estimating the error based on the residual between the forward model and the klipped data. The spectrum error term is fairly well behaved for all three planets, in general flattening with k_{klip}. The H band data taken during the survey in 2016 has more rotation and was taken after several upgrades to the instrument. It shows the most stable behavior with k_{klip}, especially for planets c and d. The behavior of the two error metrics for
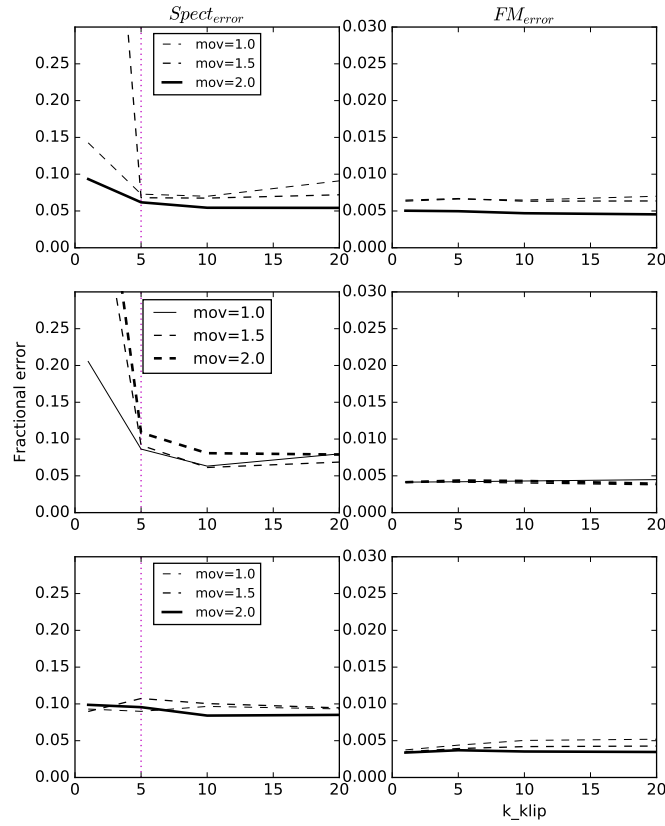
Planet e: H, K1, and K2 by row

Figure 3. Same as Figure 1, but for planet e. The solid line denotes the chosen *mov* value. k_{klip} is chosen to minimize the bias at the selected value of *mov* (pixels).

planet e improved when slices from the band edges were removed prior to PSF subtraction. We have excluded fake injections within 30 degrees of our planet location for e to avoid contamination from the planet signal.
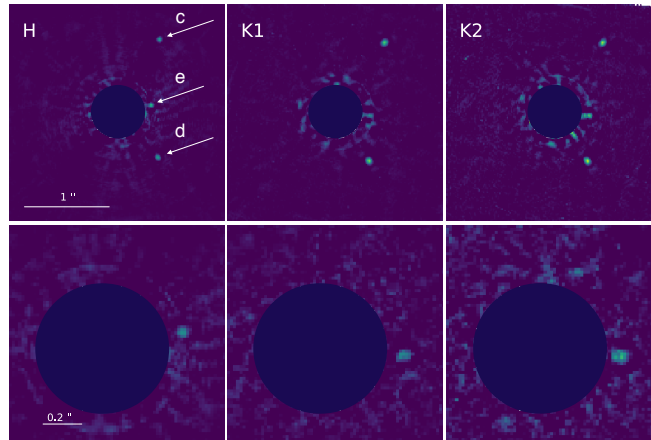

Figure 4. Top: Our KLIP subtracted cubes showing a movement of 3 pixels. **Bottom:** Subtracted cubes using a movement of 1 pixel. The data are zoomed in to highlight HR8799e.

For planets c and d we note that most of the parameter combinations yield similar level of error, within a few percent. Changing the klip parameters near our chosen values do not have a large affect on the spectrum. For planet e the bias is generally higher (note the scale in Figure 3). This is reflected in the larger errorbars for e reported in
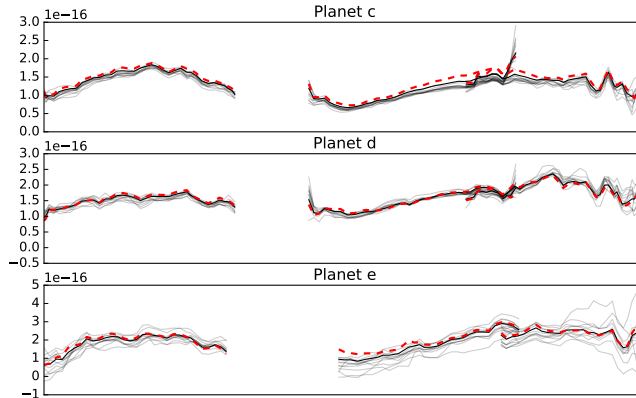
Figure 5. KLIP-FM spectrum extraction of each planet (solid black line) and recovery of fake injections (gray lines) with matching spectrum. The red dotted line shows the adjusted spectrum assuming a flux loss factor = spectrum / mean(fake spectra).

our final spectrum. We display our collapsed datacubes reduced through `PyKLIP` in Figure 4 showing a less aggressive reduction (movement=3 pixels) used to extract spectra of HR8799 c and d in the top panel, and more aggressive reduction (movement=1 pixel) used to extract the spectrum of HR8799 e in the bottom row.

3. RESULTS USING OPTIMIZED KLIP PARAMETERS

After inspecting an initial reduction with all data, we remove slices at the ends of each cube where the signal is low. This is usually due to low throughput at band edges. KLIP errors are computed from the standard deviation of the fake injection recovery at each wavelength channel. Errorbars displayed reflect contributions from the KLIP errors (σ_{fakes}) and the uncertainty in the spot flux.

We suspect that we are underestimating the flux for planet c based on the recovery of the fake injections. In Figure 5 we show the the recovered spectrum and the recovered fake injections. For c, especially at the peak, the fake spectra all lie below the recovered one, showing a systematic loss in flux over certain wavelengths. We have adjusted the spectrum (red dotted line in Figure 5) by the factor between the recovered spectrum and the mean fake spectrum.

$$\frac{f_c}{\sum f_{fake,c}/n_{fakes}}$$

In the case of both d and e, the mean fake spectrum is close to the recovered one, so we only apply this factor in the case of c.

As in Bonnefoy et al. (2016), we use a Kurucz spectrum at 7500K, matched to the photometry of HR8799A, to convert contrast to flux. We display results for the best KLIP parameters in Figure 6, adjusting our spectrum for c as indicated in Figure 5. Light blue lines for c and d panels are the K band spectra from the same dataset previous published in Ingraham et al. (2014). In black are SPHERE YJH spectra published by Bonnefoy et al. (2016) and blue squares show SPHERE photometry.

Our K-band spectrum for planet e changed the most with varying klip parameters. We note a discrepancy between the overlapping edges of our K1 and K2 spectra for e. This is unlikely to be a calibration error since it is not seen in the cases of the c and d spectra. Based on both previous photometry and our residual errors (see Appendix A), we suspect we are overestimating the flux at the edge of K1. There is possibly. The K2 spectrum of e more closely resembles that of d.

We find very similar morphology as the previously published spectra for c and d, although slightly lower flux in the case of c. Since these planets are so bright we may still be over-subtracting, if the linear approximation in the forward model is not appropriate, as described in Pueyo (2016). The SPHERE K1/K2 photometry also indicate this may be the case. Ingraham et al. (2014) noted the K-band spectra in particular, combined with photometry at 3 and 4 μm showed a lack of methane absorption, and our re-reduction is consistent. They noted the flatter spectrum for d, which also appears to be the case for our new H-band spectra compared with c and e.

The SPHERE IRDIS H-band photometry are discrepant with our result, however, these photometry are also discrepant with the SPHERE IFS spectra. Our KLIP-FM H-band spectra for d and e are in good agreement with those
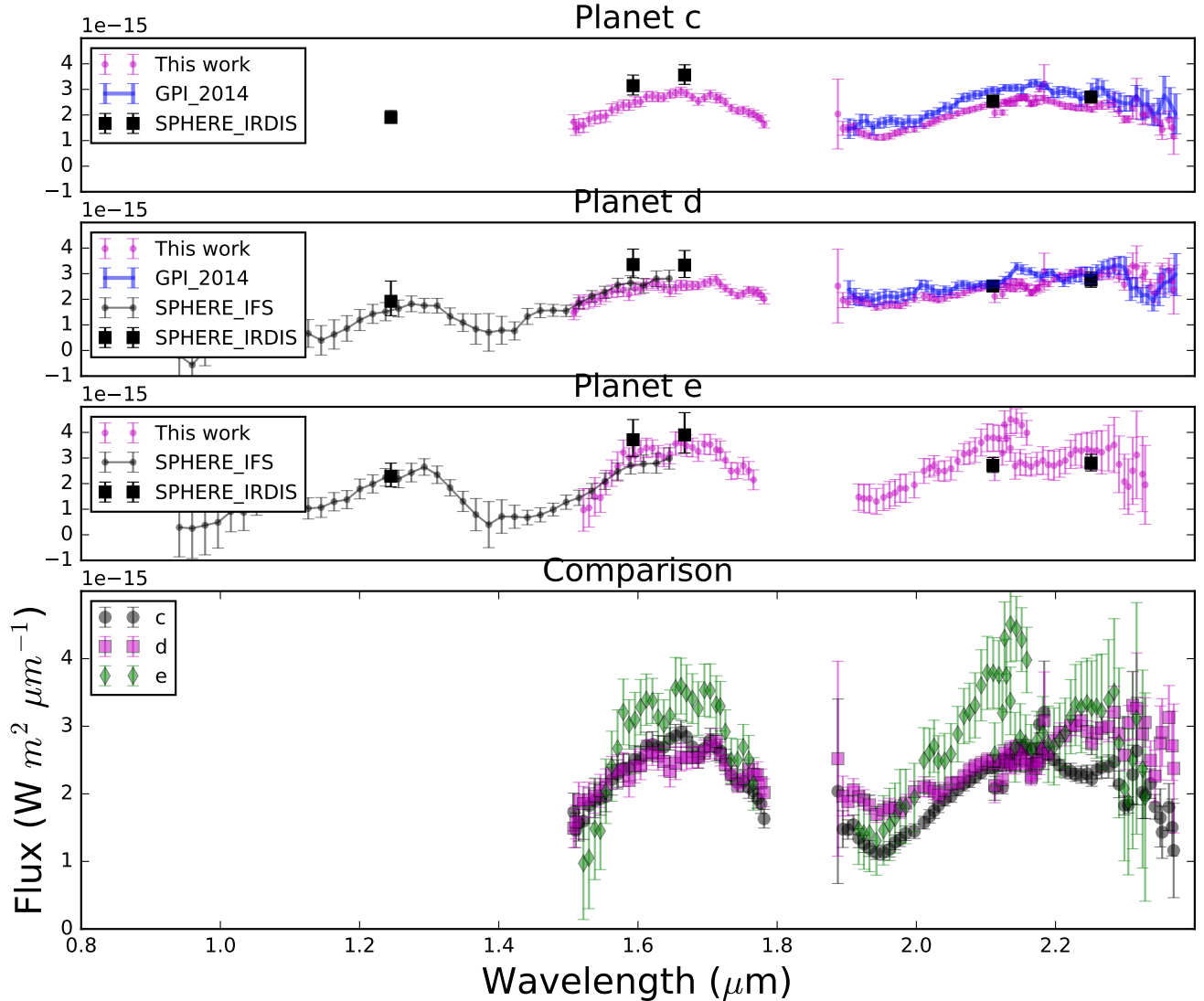
Figure 6. Spectra recovered with KLIP FM for HR8799 c, d, and e. Overplotted are the original GPI K-band spectra of c and d for the same dataset in blue (Ingraham et al. 2014), Y-H spectra (Bonnefoy et al. 2016) and Y-K photometry (Zurlo et al. 2016) using the VLT/SPHERE instrument in black points and squares. The bottom panel shows a comparison of our three recovered spectra.

obtained from the SPHERE IFS, within errorbars. Towards the center of H band we see a slight dip in the spectrum for planet e, between 1.6 and 1.7 μm, which is not seen in the SPHERE IFS spectrum. Y and J observations of HR8799 with GPI will improve the comparison and provide a complete Y-K spectra on the same instrument.

3.1. Comparison of c, d, and e

We also compare the three H-K spectra with each other to see how different they are. In the bottom panel of Figure 6 we plot all three spectra on the same axes. The H band spectrum of e appears to be most discrepant from the other two, and there are differences between all three in K1-K2. We note that our K1 and K2 spectra for e do not match. Low throughput at band edges could contribute to this discrepancy. The K2 edge suggests similarity to d.

These small differences motivate a more quantitative comparison. We compute χ^2 between each spectrum and a spectrum drawn randomly from its error:

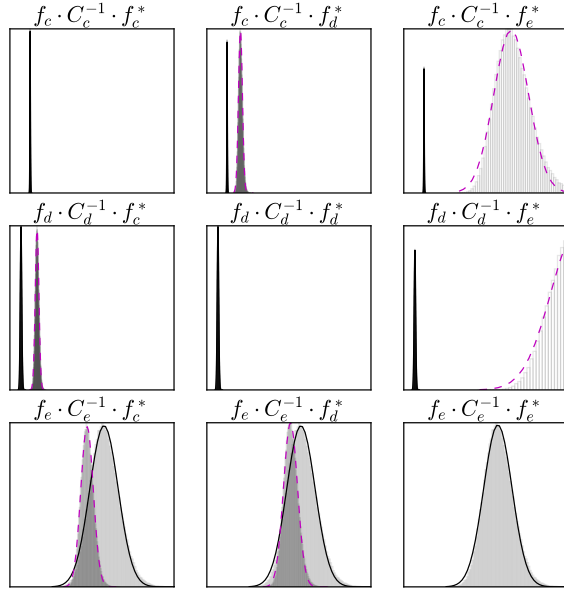$$\chi_{i,j}^2 = (f_i - f_j^*)^T C_i^{-1} (f_i - f_j^*) \tag{4}$$

Figure 7. A cross-comparison of all three planets showing the distribution of $\chi^2_{i,j}$ (defined in Equation 4) where i indicates the row and j indicates the column. The diagonal shows each spectrum compared with 10^6 random draws from itself within the errorbars. These, in solid outline are repeated for each panel in the same row. The off-diagonal panels also show the comparison with random draws from a different object spectrum, as indicated by the panel title.

where f is the spectrum of the ith object, and f^*_j is a spectrum drawn randomly from the spectrum of the jth assuming Gaussian errors, taking into account covariance C_j. C_i and C_j are the covariance matrices of the ith and jth planets computed as described in Greco & Brandt (2016) and De Rosa et al. (2016). We draw f^*_j 10^6 times for each band recompute this statistic to compare distributions.

We plot the histograms of χ^2 in Figure 7. The full spectrum comparison in is the sum of the three bands. In Appendix B we also include each comparison for H, K1, and K2 bands separately. The solid outline histogram in each panel represents the $i = j$ case, comparing each spectrum with one randomly drawn from the same spectrum. The histogram outlined in dashed lines represents the cross-comparison with a different spectrum indicated by the title of each panel. The results show a discrepancy between c and d to $> 5\sigma$. While the c-e comparison is discrepant, the e-c comparison does not show a significant discrepancy. Reducing the errors for the planet e spectrum could improve this comparison. Similarly planets e and d are not significantly distinct in the e-d comparison, showing a large amount of overlap in their distributions. Resolving the discrepancy between K1 and K2 bands edges should also improve the comparison.

3.2. *Comparison to field objects*

We compare our results with known field objects as described in Chilcote et al. (2017). We compare our H-K spectrophotometry with a library of spectra for M,L and T-dwarf field objects. These are compiled from the SpeX Prism library (Burgasser 2014), the IRTF Spectral Library (Cushing et al. 2005), the Montreal Spectral Library (Gagné et al. 2015; Robert et al. 2016), and from Allers & Liu (2013). Each spectrum and uncertainty was binned to the spectral resolution of GPI ($R \sim 45 - 80$ increasing from H to K2). We convolve the spectrum with a Gaussian function of width matching the resolution for that band. The uncertainties are normalized by the effective number of spectral channels within the convolution width.

Spectral type classifications were obtained from various literature sources, specified for individual objects. For objects that had both optical and near-IR spectral types, the near-IR spectral type was used. Gravity classifications were assigned from the literature as either old field dwarfs (α, FLD-G), intermediate surface gravity (β, INT-G), or low surface gravity, such as typically seen in young brown dwarfs (γ, δ). Several studies (Kirkpatrick 2005; Kirkpatrick et al. 2006; Cruz et al. 2009) outline the α, β, γ classification scheme, including an additional δ classification from Kirkpatrick (2005) to account for even lower gravity features. FLD-G, INT-G, VL-G follows (Allers & Liu 2013).
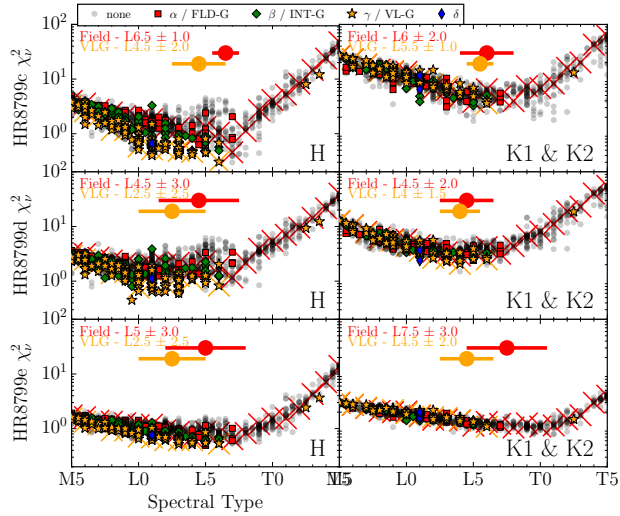
Figure 8. We plot χ^2_ν between our GPI spectrum and each object in the spectral libraries described, as a function of spectral type of field objects for each planet. From top to bottom we plot planets c, d, and e. The left shows χ^2 for H band, the right shows the χ^2 for combined K1, K2 bands. We indicate gravity classification by the legend at the top. Spectral standards for FLD-G (Burgasser 2014; Kirkpatrick et al. 2010) and VL-G (Allers & Liu 2013) are indicated by red and yellow crosses, respectively.

First we compare our spectra with those of each object in the compiled library, separately for H and K1-K2 bands. We compute reduced χ^2 using the binned spectra of comparison objects. The results for each of HR8799 c-e are shown in Figure 8. Spectral standards are marked for gravity classification where the classification is known.

Next we simultaneously fit both H, K1, and K2 bands by computing χ^2 between the spectrum of each object in these libraries and our GPI spectra, in an *unrestricted* and *restricted* fit. The unrestricted fit is done with independent normalization between bands and summing χ^2 for each band. For the restricted fit the normalization can only vary within the uncertainty in the photometric calibration (Maire et al. 2014). These are displayed in Figure 10. The definition of χ^2 in the restricted fit is described in Chilcote et al. (2017); we repeat it here for clarity:

χ^2 comparison between each of our spectra and the kth object in the library is defined as follows:

$$\chi^2_k = \sum_{j=0}^{2} \sum_{i=0}^{n_j} \left[\frac{F_j(\lambda_i) - \alpha_k \beta_{j,k} C_{j,k}(\lambda_i)}{\sqrt{\sigma^2_{F_j}(\lambda_i) + \sigma^2_{C_{j,k}}(\lambda_i)}} \right]^2$$
$$+ \sum_{j=0}^{2} \left[\frac{\beta_{j,k} - 1}{\sigma_{m_j}} \right], \tag{5}$$

summed over j bands and n_j wavelength channels in each band. $F_j(\lambda_i)$ and $\sigma_{F_j}(\lambda_i)$ are the measured flux and uncertainty in the jth band and ith wavelength channel. $C_{j,k}$ and $\sigma_{C_{j,k}}(\lambda_i)$ are the corresponding binned flux and uncertainty of the kth object. α_k is a scale factor that is the same for each band and $\beta_{j,k}$ is a band-dependent scale factor, chosen to minimize this term. The first term represents the unrestricted χ^2, where each band can vary freely by scaling factor $\beta_{j,k}$. The second cost term compares $\beta_{j,k}$ to the satellite fractional spot flux uncertainty measured in each band (Maire et al. 2014).

Lastly, we show the best fit object spectrum from our spectral library overplotted on the GPI spectra in Figure 11. We show these for both unrestricted and restricted cases. The object names, spectral types, and reduced χ^2 are displayed.

In general, each object is best represented by a mid-to-late L-type spectrum. A lack of spectral standards for gravity indicators for late L-types limits the gravity classification based on these fits, so we only report the fits to field objects. The unrestricted and restricted fits generally agree for spectral type. For the unrestricted fit the same object provides the best fit for both c and e.

Planet c is consistent with spectral type $\sim$ L6, both for the individual band fits and the simultaneous fits. The fits to low gravity types indicate earlier spectral type, but likely due to a lack of spectral standards for late L to T-type
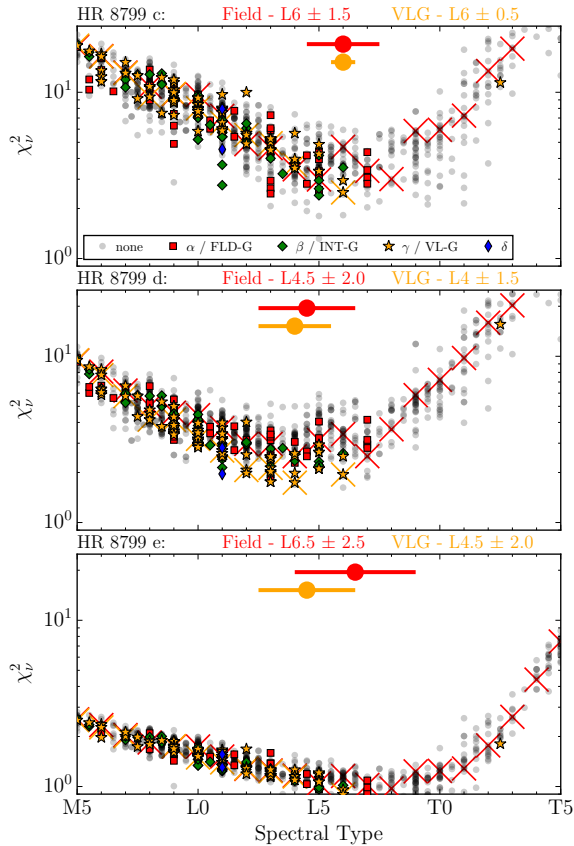
Figure 9. Unrestricted: We plot χ^2 between our combined H-K GPI spectra and each object in the library, as a function of spectral type Top to bottom we plot planets c, d, and e. The unrestricted fit allows the normalization to vary between H and K1+K2 bands.

objects. The H-band spectrum fit, in particular, indicates low gravity (yellow stars). Both unrestricted and restricted fits yield a spectral type L6.0±1.5 for planet c. The best fit object for both fits is 2MASS J10390822+2440446, which has spectral type L5 (Zhang et al. 2009).

In the case of planet d, the H band spectrum is less peaked. Spectral type ~L4.5 is best fit for both individual bands and simultaneous fits. Again, the H-band fit tends to favor low gravity. The simultaneous fit gives spectral type L4.5±2.0 for field and L4 ±1.5 for VLG objects, for both the unrestricted and restricted cases. The best fit object in both cases, 2MASS J00360925+2413434, spectral type L6 (Chiu et al. 2006; Schneider et al. 2014).

The individual H and K fits are flatter for e. The H-band and K-band individual fits are consistent with mid-to-late L-type spectrum. The K-band part of the spectrum is consistent with a wide range of spectral types, extending to early T, due in part to large errorbars. The simultaneous fit gives spectral type L6.5±2.5 for the unrestricted fit and L6±2.0. Both restricted and unrestricted cases yield the best fit for 2MASS J1049-5319A, (Luhman 2013) classified as type L7.5 Burgasser et al. (2013).

Better wavelength coverage would improve spectral type fitting, as well as a larger library of mid-IR spectra and photometry for comparison objects from the field. More low-gravity standards at late spectral types would also also improve the VLG fits. Resolving the discrepancy at the edge of K1 and K2 would also help constrain its best fit spectral type.

3.3. Comparison to model spectra

We compare our HR8799 c,d,e spectra with several atmospheric models that have been presented in previous studies to fit the planet spectra and/or photometry. We consider atmosphere models from Barman et al. (2011) (PHOENIX),
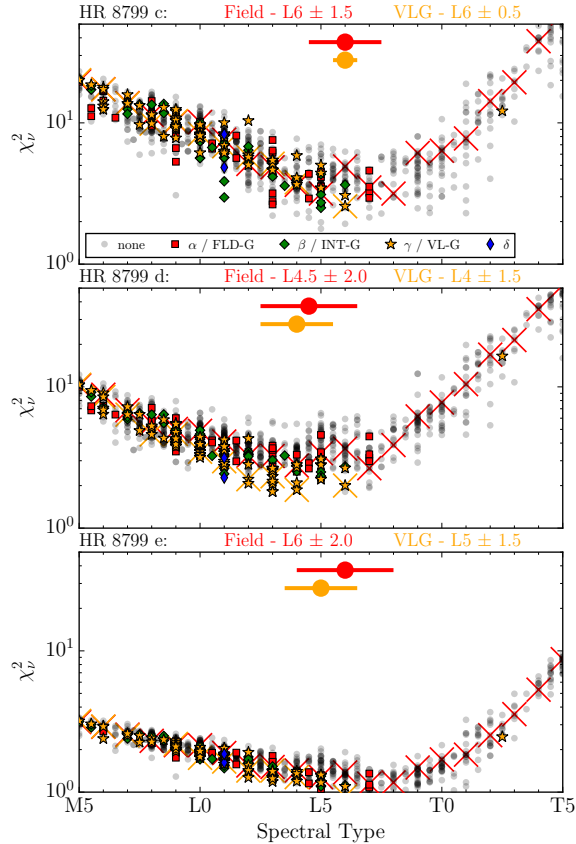
Figure 10. Restricted: We plot χ^2 between our combined H-K GPI spectra and each object in the library, as a function of spectral type Top to bottom we plot planets c, d, and e. The restricted fit only allows the normalization to vary within the uncertainty of photometric calibration.

Saumon & Marley (2008), Madhusudhan et al. (2011)[2] and Baraffe et al. (2015)[3]. For each set of models, we convolve the model spectrum with a Gaussian to match the spectral resolution of GPI in H-band, and interpolate to the same wavelengths of the GPI spectrum. We adjust the radius so that it minimizes χ^2 between the model and our spectra. The models are only matched to our H and K spectra. We also show broadband photometry (Marois et al. 2008, 2010b; Galicher et al. 2011; Currie et al. 2011; Skemer et al. 2012, 2014; Currie et al. 2014; Zurlo et al. 2016), previously compiled in Bonnefoy et al. (2016), leaving out SPHERE H-band points, which are discrepant. Table 2 summarizes model parameters fit to each planet. Figure 12 displays each model presented in the table alongside our spectrum and photometry from literature. Each set of models is discussed in detail in the following sections.

3.3.1. *PHOENIX model*

The PHOENIX (v16) models from Barman et al. (2011) is a set of parameterized models with clouds, where clouds consist of a complex mixture or particles whose state depend on temperature and pressure. This set of models takes into account the transition between cloudless and cloudy atmosphere, as seen between L- and T-type objects. This aim model is designed to identify the major physical properties of the atmosphere. Given degeneracies in the model between parameters such as gravity, temperature, and cloud thickness, Konopacky et al. (2013) fit wavelength ranges and features that were most sensitive to each parameter to provide an overall best fit, checking consistency with broadband photometry. A combination of dynamical stability, age, and interior structure models restricted the fit to $\lesssim 3.5 < \log g \lesssim 4.4$ and $900K \lesssim T_{eff} \lesssim 1300K$, leading to a model at $\log g = 4.0$ and T_{eff}=1100K, moderate cloud thickness, a large eddy diffusion coefficient $K_{zz} = 10^8 cm^2 s^{-1}$, and super-solar C/O.

---

[2] http://www.astro.princeton.edu/~burrows/8799/8799.html

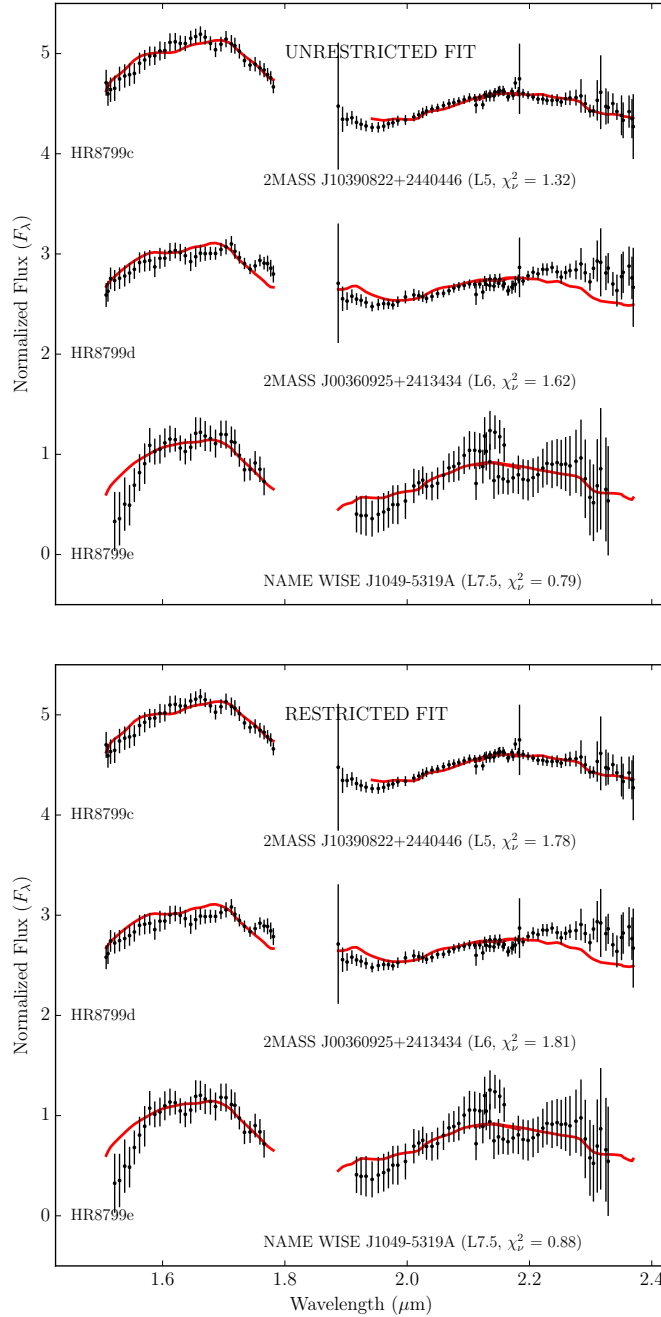[3] https://phoenix.ens-lyon.fr/Grids/BTSettl/CIFIST2011_2015/

Figure 11. Best fit object to each of HR8799 c, d, and e spectra within the described spectral library. The top panel shows the unrestricted best fit spectrum to each planet (Zhang et al. 2009; Chiu et al. 2006; Schneider et al. 2014). The bottom shows the restricted best fit, matching the unrestricted best fit for c and d, and indicating a different best fit for e (Chiu et al. 2006).

We compare this tuned model, normalized (by scaling the radius) to fit each spectrum. We show this alongside other models in Figure 12. We expect it to match the c spectrum best, since it was tuned to fit the Keck/OSIRIS spectrum of c (Konopacky et al. 2013). The comparison highlights different features of the three spectra.

The best fitting model from Konopacky et al. (2013) should be most appropriate for c, and does a good job matching both the H and K spectra. The spectrum for d is least similar to this model, especially with a flatter H-band spectrum and rising slope in K band. It is possibly better represented by a higher effective temperature as with the BT-Settl model we will show in §3.3.4. The model reasonably fits the spectrum for e, within the large errorbars. This model, fit to our H-K spectrum is most consistent with the $3 - 5\mu m$ photometry in all 3 cases.
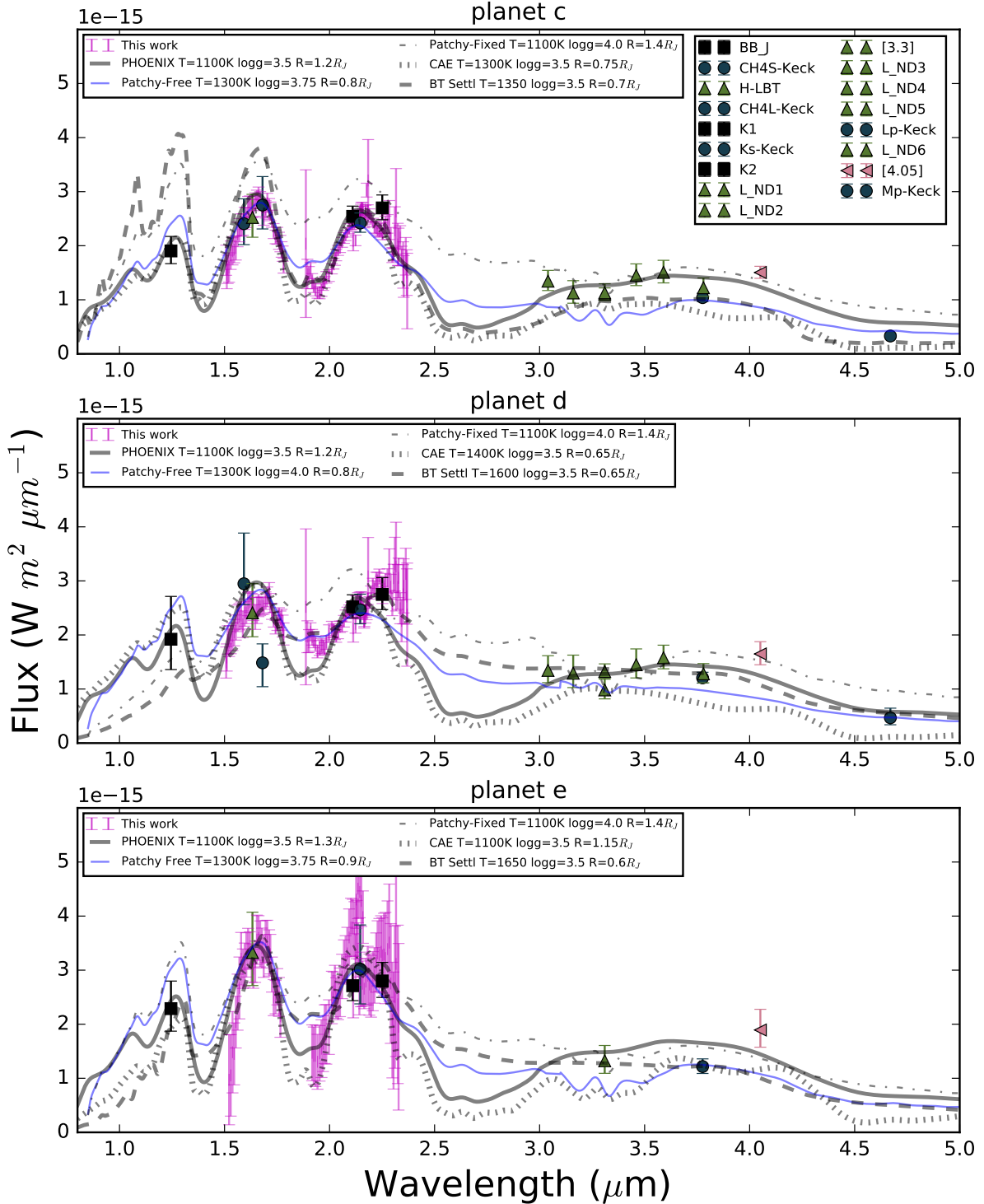
Figure 12. Atmospheric models are plotted in various line styles indicated by the legend for HR8799 c (top), d (middle), and e (bottom). GPI spectra are plotted as magenta bars. Normalized Phoenix models is displayed with a a thick gray line. The normalized patchy cloud models are plotted in thin solid blue lines, while the fixed patchy cloud models are plotted in dash-dot lines. Cloud-AE models are plotted as a dotted line, and BT-Settl models as dashed lines. We also plot broadband photometry from previous work, with symbols corresponding to each instrument. Black squares correspond to VLT/SPHERE IRDIS (Zurlo et al. 2016), teal circles to Keck/NIRC2 (Marois et al. 2008, 2010b; Galicher et al. 2011; Currie et al. 2011), green vertical triangles to LBT (Skemer et al. 2012, 2014), and pink left-pointing triangles to NACO (Currie et al. 2014).

3.3.2. *Patchy cloud model*

Models from Saumon & Marley (2008) are evolution models for brown dwarfs and giant planets in the "hot start" scenario that include patchy clouds. These are parameterized based on effective temperature, cloud properties (cloud hole fraction), gravity, and mixing properties, namely a sedimentation parameter f_{sed} defined in Ackerman & Marley (2001), the ratio between the sedimentation velocity and the convective velocity scale. These models have solar abundance, which may not be a valid assumption. Previous atmospheric retrieval studies have suggested a super-solar metallicity could reproduce the photometry and spectroscopy for at least a subset of the HR8799 planets (Lee et al. 2013; Lavie et al. 2017).

Ingraham et al. (2014) found that while models are able to reproduce the planet SEDs, they are not consistent with the more detailed spectra, and in some cases require unrealistically small radii. Modeling these objects may require a combination of cloud opacity, cloud holes, disequilibrium chemistry, and non-solar metallicity to reproduce both the observed photometry and spectroscopy. Two sets of models were tested, one with fixed radius based on hot-start evolutionary models, and another where the radius was allowed to vary independent of T_{eff} and log g. We display the same four models discussed in Ingraham et al. (2014) in Figure 12, in solid thin (free) and dash-dot (fixed) lines.

The first set of models at 1100K have thick clouds with some horizontal variation, to allow the observed J-band flux. The fixed model chosen for c has f_{sed} of 0.25 and cloud hole fraction of 5%. The fixed model chosen for d has f_{sed}=0.50 and no holes. Of these two, the former provides a better fit for e. When radius was allowed to vary models at 1300K best represented the spectra for both c and e. This model has f_{sed}=1, without cloud holes. The varying model at 1300K with $f_{sed} = 0.5$ and 5% holes best fits the spectrum for d.

As in Ingraham et al. (2014) we find the fixed-radius models do not provide a good fit of the spectra and that sub-Jupiter radii are required T_{eff} =1300K models. For c, fitting both the H and K spectrum for the best scaling leads to a poorer fit of the K-band portion. In the case of d neither model fits the flatter H-band spectrum, nor the rising in K2. For e, the fixed-radius model at 1100K reproduces the peak flux at H and K but does not capture the band edges. In general, the models do not capture the relative flux between H and K for all three objects. The fits to the H-K spectra when the radius is allowed to vary under-predicts photometry at 3-5μm.

3.3.3. *CloudAE-60 model grid*

Next, we consider the CloudAE-60 model grid (Madhusudhan et al. 2011), also discussed in Bonnefoy et al. (2016). These models represent thick forsterite clouds at solar metallicity with mean particle size of 60μm. These models do not account for disequilibrium chemistry. We fit the grid of models between 1100 and 1600K and radius scaling. In Figure 12 we plot the CloudAE-60 model at effective temperature and radius that minimizes χ^2 in dotted lines.

Table 2. Best fitting models

Planet	Model	Radius	T_{eff} (K)	log(g)
HR8799 c	PHOENIX (v16)	1.2	1100	3.5
	Saumon+ (2008) *fixed*	1.4	1100	4.0
	Saumon+ (2008)	0.8	1300	3.75
	Cloud-AE60	0.75	1300	3.5
	BT-Settl	0.7	1350	3.5
HR8799 d	PHOENIX (v16)	1.2	1100	3.5
	Saumon+ (2008) *fixed*	1.4	1100	4.0
	Saumon+ (2008)	0.8	1300	4.0
	Cloud-AE60	0.65	1400	3.5
	BT-Settl	0.65	1600	3.5
HR8799 e	PHOENIX (v16)	1.3	1100	3.5
	Saumon+ (2008) *fixed*	1.4	1100	4.0
	Saumon+ (2008)	0.9	1300	3.75
	Cloud-AE60	1.15	1100	3.5
	BT-Settl	0.6	1650	3.5

This set of models is able to reproduce the K-band spectra of c and e fairly well all the way to band edges. The model does not match the shape of the d spectrum, neither representing the flatter H-band spectrum, nor the rising K-band spectrum. We find similar best fitting effective temperature for e as in Bonnefoy et al. (2016). All three cases produce models that require radii below 1 R_{Jup}. The models that best-fit the H-K spectra do not match the flux at 3-5 μm.

3.3.4. *BT-Settl model grid*

Lastly, the BT-Settl 2014 evolutionary model grid for low mass stars couples atmosphere and interior structures (Baraffe et al. 2015). We consider a temperature range from 1200 - 1700K and gravity range logg =3.0 - 4.0, encompassing the best fits shown in Bonnefoy et al. (2016). The grid provides models in steps of 100K; to estimate intermediate temperatures, we average models to search in steps 50K. We show these best fits in dashed lines along with the other models in Figure 12.

We find similar best fits for c and d as Bonnefoy et al. (2016). This model better reflects the rising slope in K for planet d and in this case is roughly consistent with photometry beyond 3μm. This set of models also under-predict flux from 3-5μm in some cases. Bonnefoy et al. (2016) similarly noted that this model did not both match Y-H spectra and the 3-5 μm flux, possibly indicating that it does not produce enough dust at high altitudes. In both studies this model matches the planet d photometry better than for c.

4. SUMMARY AND CONCLUSIONS

We have implemented the forward modeling approach to recovering IFS spectra from GPI observations of HR8799. Using this approach we have re-reduced data first presented in Ingraham et al. (2014) with this new algorithm. We also present new H-band for HR8799 c, d, and e, as well as the first K-band spectra for HR8799e. The HR8799 planet SEDs have been typically shown to be very similar, but differences in the spectra could indicate different atmospheric properties (cloud fraction, non-equilibrium chemistry and composition) and/or bulk properties (effective temperature, gravity). Planet c and d are distinct. With less noisy K-band data we could make a stronger statement about difference between planet e and the other planets in the system. The H-band spectrum for e may be brighter than the others, especially with respect to the K band. It is likely the K-band spectrum for e resembles that of d and that our K1 band edge is overestimating the flux. **(Any additional comment on the significance of H band vs. K-band differences wrt cloud properties/ processes/ composition/ etc?)**.

The following points summarize our results:

- Algorithm parameters can be chosen based on minimizing error in the spectrum by recovering simulated sources, over a range of algorithm parameters.

- The new H spectra of planets d and e are consistent at the short end with YJH spectra recently published from the SPHERE/VLT instrument(Bonnefoy et al. 2016).

- The H-K spectrum of HR8799c is statistically different ($> 5\sigma$) from d based on our $\chi^2_{i,j}$ measurement.

- All three objects are best matched by mid to late L-type field brown dwarfs from a library of spectral standard.

- The PHOENIX model, based on non-equilibrium chemistry, seems to best reproduce both the H-K spectra and the 3-5 μm photometry for planets c and e, without requiring unrealistic radii. It's important to note that this model was carefully tuned to match the the K band spectrum of planet c in as well as its 3-5μm flux (Konopacky et al. 2013). A general grid of models is not expected to provide this level of detailed fit, however the CloudAE models produce very similar results from H-K.

- In the case of d, the BT-Settl models seem to represent the H-K spectra the best, while also matching the 3-5μm photometry, but still requires a sub-M_{Jup} radius.

Generalized model grids are more likely to provide a rough fit, and may produce some unrealistic parameters, such as sub-Jupiter radii. As we see in the case of the HR8799 planets, despite similar SEDs, the more detailed spectra show clear differences between them. A new set of dedicated models could help explain differences in composition and atmospheric processes between the HR8799 planets, especially accounting for effects like non-equilibrium chemistry,

clouds, and/or non-solar metallicity. Larger spectral coverage could also help inform new models or atmosphere retrieval.

JWST will be able to deliver spectra at longer wavelength. With lower thermal background, it will help to better characterize planetary mass companions at 3-5μm and beyond. Given the reduced diameter compared to ground-based 8m-class telescopes, forward modeling may be important for obtaining infrared companion spectra to systems like HR8799, helping to advance modeling efforts and provide benchmark objects for future high contrast imaging studies.

This research has made use of the SVO Filter Profile Service (http://svo2.cab.inta-csic.es/theory/fps/) supported from the Spanish MINECO through grant AyA2014-55216. This research has benefited from the SpeX Prism Library maintained by Adam Burgasser at http://www.browndwarfs.org/spexprism

Facilities:

Facility: Gemini-S.

Software: PyKLIP (Wang et al. 2015), astropy (Astropy Collaboration et al. 2013), matplotlib (Hunter 2007), Numpy (Van Der Walt et al. 2011)

APPENDIX

A. A: RESIDUALS

After optimizing KLIP parameters, described in section 2.2, we display the PSF-subtracted data stamp that contains the planet and the forward model, summed over the bandpass, and the residual between the two (Figure 13). We show the residual plots for all three planets in each H, K1, and K2 bands, summed over the wavelength axis.
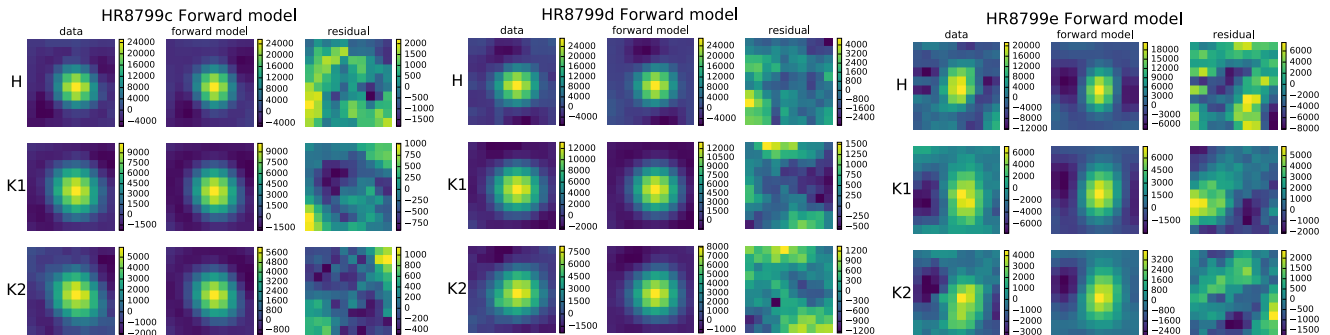
Figure 13. A summary of the forward model performance for planet c (left) d (middle) and e (right). Sum over each bandpass of klipped data (left) and the forward model (middle). The rightmost panel shows the difference between these two. Pixel values are in raw data units.

Noisiness close to the center of the image contributes larger residuals for the forward model of planet e. However, as can be seen in the Figure 13, the forward model captures the self-subtraction negative lobes. We have taken care to remove obvious contaminants, like a bad pixel in several wavelength channels near HR8799d.

B. SPECTRUM COMPARISON BY BAND

We show the individual spectra comparisons between HR8799c, d, and e. The compiled figure in the main text is the addition of all three of these plots.

The H-band comparison shows that the spectrum for e is distinct from the other two, which is also obvious by qualitative inspection. The spectrum of planet e is overall brighter in the middle of the band, and is not smooth like the other two.

The K1 spectra show the largest distinction between planet c and d and between c and e. Here, planet e is most closely similar to planet d. For K2 band the spectra of c and d are still distinct but less-so. There is considerable overlap between c and e and between e and d. Some of this is likely due to the large errorbars for the spectrum of e.
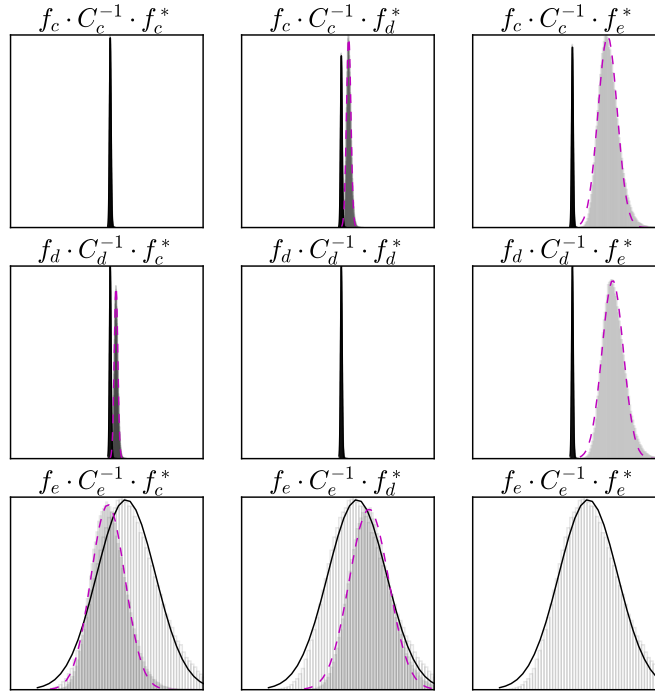
GREENBAUM ET AL.

$$f_c \cdot C_c^{-1} \cdot f_c^*$$ $$f_c \cdot C_c^{-1} \cdot f_d^*$$ $$f_c \cdot C_c^{-1} \cdot f_e^*$$

$$f_d \cdot C_d^{-1} \cdot f_c^*$$ $$f_d \cdot C_d^{-1} \cdot f_d^*$$ $$f_d \cdot C_d^{-1} \cdot f_e^*$$

$$f_e \cdot C_e^{-1} \cdot f_c^*$$ $$f_e \cdot C_e^{-1} \cdot f_d^*$$ $$f_e \cdot C_e^{-1} \cdot f_e^*$$

Figure 14. Comparison of χ^2 distributions for H band.

$$f_c \cdot C_c^{-1} \cdot f_c^*$$ $$f_c \cdot C_c^{-1} \cdot f_d^*$$ $$f_c \cdot C_c^{-1} \cdot f_e^*$$

$$f_d \cdot C_d^{-1} \cdot f_c^*$$ $$f_d \cdot C_d^{-1} \cdot f_d^*$$ $$f_d \cdot C_d^{-1} \cdot f_e^*$$

$$f_e \cdot C_e^{-1} \cdot f_c^*$$ $$f_e \cdot C_e^{-1} \cdot f_d^*$$ $$f_e \cdot C_e^{-1} \cdot f_e^*$$
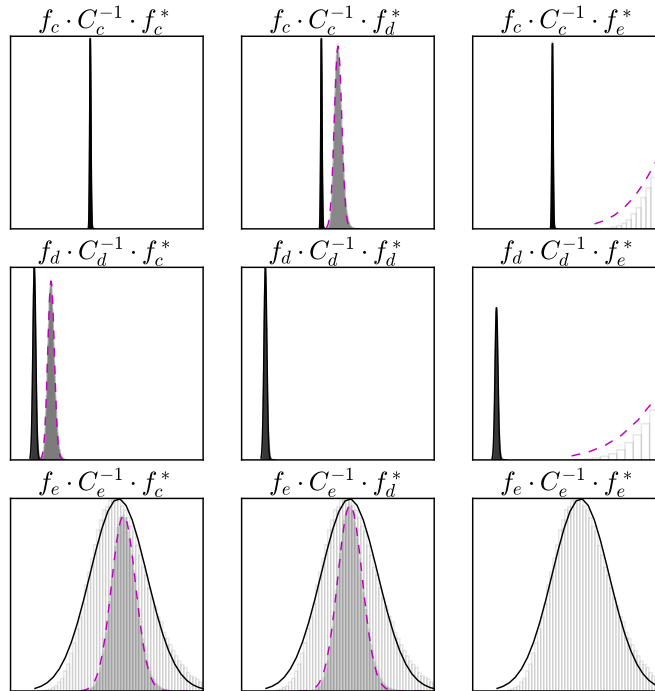
Figure 15. Comparison of χ^2 distributions for K1 band.

REFERENCES

Ackerman, A. S., & Marley, M. S. 2001, ApJ, 556, 872,
    doi: 10.1086/321540

Allers, K. N., & Liu, M. C. 2013, ApJ, 772, 79,
    doi: 10.1088/0004-637X/772/2/79

$f_c \cdot C_c^{-1} \cdot f_c^*$ $f_c \cdot C_c^{-1} \cdot f_d^*$ $f_c \cdot C_c^{-1} \cdot f_e^*$

$f_d \cdot C_d^{-1} \cdot f_c^*$ $f_d \cdot C_d^{-1} \cdot f_d^*$ $f_d \cdot C_d^{-1} \cdot f_e^*$

$f_e \cdot C_e^{-1} \cdot f_c^*$ $f_e \cdot C_e^{-1} \cdot f_d^*$ $f_e \cdot C_e^{-1} \cdot f_e^*$
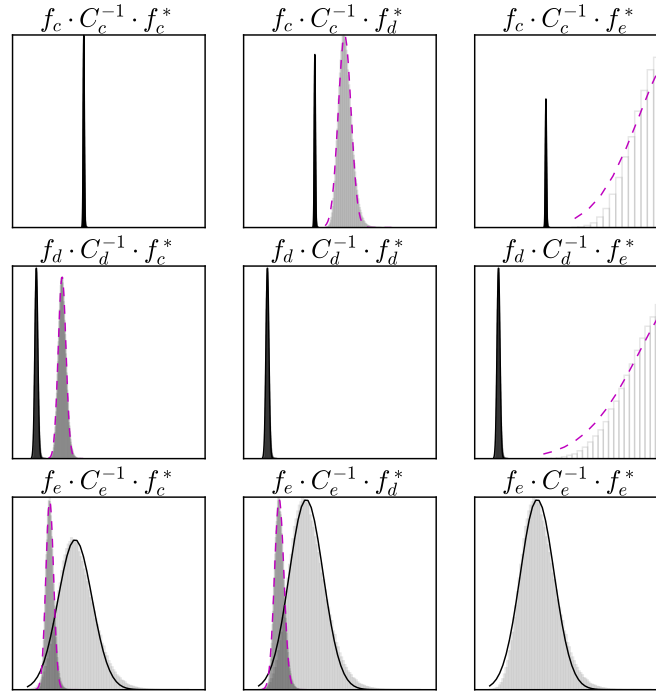
Figure 16. Comparison of χ^2 distributions for K2 band.

Apai, D., Kasper, M., Skemer, A., et al. 2016, ApJ, 820, 40, doi: 10.3847/0004-637X/820/1/40

Astropy Collaboration, Robitaille, T. P., Tollerud, E. J., et al. 2013, A&A, 558, A33, doi: 10.1051/0004-6361/201322068

Baraffe, I., Homeier, D., Allard, F., & Chabrier, G. 2015, A&A, 577, A42, doi: 10.1051/0004-6361/201425481

Barman, T. S., Konopacky, Q. M., Macintosh, B., & Marois, C. 2015, ApJ, 804, 61, doi: 10.1088/0004-637X/804/1/61

Barman, T. S., Macintosh, B., Konopacky, Q. M., & Marois, C. 2011, ApJ, 733, 65, doi: 10.1088/0004-637X/733/1/65

Bonnefoy, M., Zurlo, A., Baudino, J. L., et al. 2016, A&A, 587, A58, doi: 10.1051/0004-6361/201526906

Bowler, B. P., Liu, M. C., Dupuy, T. J., & Cushing, M. C. 2010, ApJ, 723, 850, doi: 10.1088/0004-637X/723/1/850

Burgasser, A. J. 2014, in Astronomical Society of India Conference Series, Vol. 11, Astronomical Society of India Conference Series

Burgasser, A. J., Sheppard, S. S., & Luhman, K. L. 2013, ApJ, 772, 129, doi: 10.1088/0004-637X/772/2/129

Chilcote, J., Pueyo, L., De Rosa, R. J., et al. 2017, AJ, 153, 182, doi: 10.3847/1538-3881/aa63e9

Chiu, K., Fan, X., Leggett, S. K., et al. 2006, AJ, 131, 2722, doi: 10.1086/501431

Cruz, K. L., Kirkpatrick, J. D., & Burgasser, A. J. 2009, AJ, 137, 3345, doi: 10.1088/0004-6256/137/2/3345

Currie, T., Burrows, A., Itoh, Y., et al. 2011, ApJ, 729, 128, doi: 10.1088/0004-637X/729/2/128

Currie, T., Burrows, A., Girard, J. H., et al. 2014, ApJ, 795, 133, doi: 10.1088/0004-637X/795/2/133

Cushing, M. C., Rayner, J. T., & Vacca, W. D. 2005, ApJ, 623, 1115, doi: 10.1086/428040

De Rosa, R. J., Rameau, J., Patience, J., et al. 2016, ApJ, 824, 121, doi: 10.3847/0004-637X/824/2/121

Fabrycky, D. C., & Murray-Clay, R. A. 2010, ApJ, 710, 1408, doi: 10.1088/0004-637X/710/2/1408

Gagné, J., Faherty, J. K., Cruz, K. L., et al. 2015, ApJS, 219, 33, doi: 10.1088/0067-0049/219/2/33

Galicher, R., Marois, C., Macintosh, B., Barman, T., & Konopacky, Q. 2011, ApJL, 739, L41, doi: 10.1088/2041-8205/739/2/L41

GPI instrument Collaboration. 2014, GPI Pipeline: Gemini Planet Imager Data Pipeline, Astrophysics Source Code Library. http://ascl.net/1411.018

Greco, J. P., & Brandt, T. D. 2016, ApJ, 833, 134, doi: 10.3847/1538-4357/833/2/134

Hinz, P. M., Rodigas, T. J., Kenworthy, M. A., et al. 2010, ApJ, 716, 417, doi: 10.1088/0004-637X/716/1/417

Hunter, J. D. 2007, Computing in Science and Engineering, 9, 90, doi: 10.1109/MCSE.2007.55

Ingraham, P., Marley, M. S., Saumon, D., et al. 2014, ApJL, 794, L15, doi: 10.1088/2041-8205/794/1/L15

Janson, M., Bergfors, C., Goto, M., Brandner, W., & Lafrenière, D. 2010, ApJL, 710, L35, doi: 10.1088/2041-8205/710/1/L35

Kirkpatrick, J. D. 2005, ARA&A, 43, 195, doi: 10.1146/annurev.astro.42.053102.134017

Kirkpatrick, J. D., Barman, T. S., Burgasser, A. J., et al. 2006, ApJ, 639, 1120, doi: 10.1086/499622

Kirkpatrick, J. D., Looper, D. L., Burgasser, A. J., et al. 2010, ApJS, 190, 100, doi: 10.1088/0067-0049/190/1/100

Konopacky, Q. M., Barman, T. S., Macintosh, B. A., & Marois, C. 2013, Science, 339, 1398, doi: 10.1126/science.1232003

Konopacky, Q. M., Marois, C., Macintosh, B. A., et al. 2016, AJ, 152, 28, doi: 10.3847/0004-6256/152/2/28

Konopacky, Q. M., Thomas, S. J., Macintosh, B. A., et al. 2014, in Proc. SPIE, Vol. 9147, Ground-based and Airborne Instrumentation for Astronomy V, 914784

Lafrenière, D., Marois, C., Doyon, R., & Barman, T. 2009, ApJL, 694, L148, doi: 10.1088/0004-637X/694/2/L148

Lagrange, A.-M., Bonnefoy, M., Chauvin, G., et al. 2010, Science, 329, 57, doi: 10.1126/science.1187187

Lavie, B., Mendonça, J. M., Mordasini, C., et al. 2017, AJ, 154, 91, doi: 10.3847/1538-3881/aa7ed8

Lee, J.-M., Heng, K., & Irwin, P. G. J. 2013, ApJ, 778, 97, doi: 10.1088/0004-637X/778/2/97

Luhman, K. L. 2013, ApJL, 767, L1, doi: 10.1088/2041-8205/767/1/L1

Madhusudhan, N., Burrows, A., & Currie, T. 2011, ApJ, 737, 34, doi: 10.1088/0004-637X/737/1/34

Maire, J., Ingraham, P. J., De Rosa, R. J., et al. 2014, in Proc. SPIE, Vol. 9147, Ground-based and Airborne Instrumentation for Astronomy V, 914785

Marley, M. S., Saumon, D., Cushing, M., et al. 2012, ApJ, 754, 135, doi: 10.1088/0004-637X/754/2/135

Marois, C., Macintosh, B., Barman, T., et al. 2008, Science, 322, 1348, doi: 10.1126/science.1166585

Marois, C., Macintosh, B., & Véran, J.-P. 2010a, in Proc. SPIE, Vol. 7736, Adaptive Optics Systems II, 77361J

Marois, C., Zuckerman, B., Konopacky, Q. M., Macintosh, B., & Barman, T. 2010b, Nature, 468, 1080, doi: 10.1038/nature09684

Öberg, K. I., Murray-Clay, R., & Bergin, E. A. 2011, ApJL, 743, L16, doi: 10.1088/2041-8205/743/1/L16

Perrin, M. D., Maire, J., Ingraham, P., et al. 2014, in Proc. SPIE, Vol. 9147, Ground-based and Airborne Instrumentation for Astronomy V, 91473J

Pueyo, L. 2016, ApJ, 824, 117, doi: 10.3847/0004-637X/824/2/117

Pueyo, L., Soummer, R., Hoffmann, J., et al. 2015, ApJ, 803, 31, doi: 10.1088/0004-637X/803/1/31

Rajan, A., Barman, T., Soummer, R., et al. 2015, ApJL, 809, L33, doi: 10.1088/2041-8205/809/2/L33

Robert, J., Gagné, J., Artigau, É., et al. 2016, ApJ, 830, 144, doi: 10.3847/0004-637X/830/2/144

Ruffio, J.-B., Macintosh, B., Wang, J. J., et al. 2017, ApJ, 842, 14, doi: 10.3847/1538-4357/aa72dd

Saumon, D., & Marley, M. S. 2008, ApJ, 689, 1327, doi: 10.1086/592734

Schneider, A. C., Cushing, M. C., Kirkpatrick, J. D., et al. 2014, AJ, 147, 34, doi: 10.1088/0004-6256/147/2/34

Sivaramakrishnan, A., & Oppenheimer, B. R. 2006, ApJ, 647, 620, doi: 10.1086/505192

Skemer, A. J., Hinz, P. M., Esposito, S., et al. 2012, ApJ, 753, 14, doi: 10.1088/0004-637X/753/1/14

Skemer, A. J., Marley, M. S., Hinz, P. M., et al. 2014, ApJ, 792, 17, doi: 10.1088/0004-637X/792/1/17

Soummer, R., Brendan Hagan, J., Pueyo, L., et al. 2011, ApJ, 741, 55, doi: 10.1088/0004-637X/741/1/55

Soummer, R., Pueyo, L., & Larkin, J. 2012, ApJL, 755, L28, doi: 10.1088/2041-8205/755/2/L28

Van Der Walt, S., Colbert, S. C., & Varoquaux, G. 2011, Computing in Science and Engineering, 13, 22, doi: 10.1109/MCSE.2011.37

Wang, J. J., Ruffio, J.-B., De Rosa, R. J., et al. 2015, pyKLIP: PSF Subtraction for Exoplanets and Disks, Astrophysics Source Code Library. http://ascl.net/1506.001

Wang, J. J., Rajan, A., Graham, J. R., et al. 2014, in Proc. SPIE, Vol. 9147, Ground-based and Airborne Instrumentation for Astronomy V, 914755

Wang, J. J., Graham, J. R., Pueyo, L., et al. 2016, AJ, 152, 97, doi: 10.3847/0004-6256/152/4/97

Wertz, O., Absil, O., Gómez González, C. A., et al. 2017, A&A, 598, A83, doi: 10.1051/0004-6361/201628730

Wolff, S. G., Perrin, M. D., Maire, J., et al. 2014, in Proc. SPIE, Vol. 9147, Ground-based and Airborne Instrumentation for Astronomy V, 91477H

Zhang, Z. H., Pokorny, R. S., Jones, H. R. A., et al. 2009, A&A, 497, 619, doi: 10.1051/0004-6361/200810314

Zurlo, A., Vigan, A., Galicher, R., et al. 2016, A&A, 587, A57, doi: 10.1051/0004-6361/201526835